

# Flow inside impeller sidewall gaps and disk friction of radial centrifugal pump

Lucie Zemanová<sup>1,\*</sup>, Pavel Rudolf<sup>1</sup>, Andrey V. Naumov<sup>2</sup>, and Alexander V. Volkov<sup>2</sup>

<sup>1</sup>Victor Kaplan Dept. of Fluid Eng., Faculty of Mech. Eng., Brno University of Technology, Technická 2, 616 69 Brno, Czech Republic <sup>2</sup>National Research University Moscow Power Engineering Institute, Moscow 111250, Russia

**Abstract.** Disk friction losses can significantly influence the overall pump efficiency. It is most pronounced in the case of machines with low or moderate specific speed, which has to be kept in mind during a design process of a pump. However, analyses using computational fluid dynamics (CFD) often completely neglect the sidewall gaps geometry. Correctly solved flow in the sidewall gaps can have a great impact on the whole flow pattern inside the pump and therefore it can considerably influence the calculated efficiency. The paper is focused on the precise simulation of the flow in the spaces between impeller shrouds and casing. CFD study using embedded Large Eddy Simulation (LES) approach in order to achieve accurate insight into the flow in sidewall gaps and reasonable computational time was performed. Obtained results are compared with data from experimental measurements.

## 1 Introduction

The disk friction losses are generated on a hub and a shroud of an impeller rotating in fluid inside a casing. It is caused by shear stress appearing on the surfaces. It can have a major impact on hydraulic efficiency drop especially in case of low and moderate specific speed pumps. According to [1], at specific speed  $n_s = 10$ , the disk friction losses consume typically to about 50 % of the useful power.

The problem of the disk friction was first studied on simplified cases, see Fig. 1 left. Plain disk rotating in cylindrical casing was extensively experimentally studied by Daily and Nece [2]. The friction moment can be expressed as:

$$M = c_m \frac{1}{2} \rho \omega^2 D^5 \quad (1)$$

where  $M$  is the friction moment,  $c_m$  is dimensionless moment coefficient dependent on flow regime,  $\rho$  is density of the fluid,  $\omega$  is angular velocity of the disk,  $D$  is the outer diameter of the disk. Considering Reynolds number ( $Re$ ), the gap width  $h$  and the disk diameter  $D$ , four flow regimes can occur:

- Regime I: laminar, merged boundary layers
- Regime II: laminar, separated boundary layers
- Regime III: turbulent, merged boundary layers
- Regime IV: turbulent, separated boundary layers

For each of the regimes, moment coefficient determining friction can be expressed by different equation [2]. Later, the study was expanded to include also an influence of surface roughness of the disk and the casing [3].

It was found out, that a presence of throughflow can change the friction in a significant way. Coren et al. [4] demonstrated it on a set of experiments with open cavity. For low level of throughflow, the flow structure inside the cavity is dominated by rotation. With increasing flow rate  $Q$ , the tangential velocity decreases, boundary layers become thinner leading to increase of the disk friction. Hu et al. [5, 6] dealt with the influence of the direction of the throughflow and correlated it to particular four flow regimes.

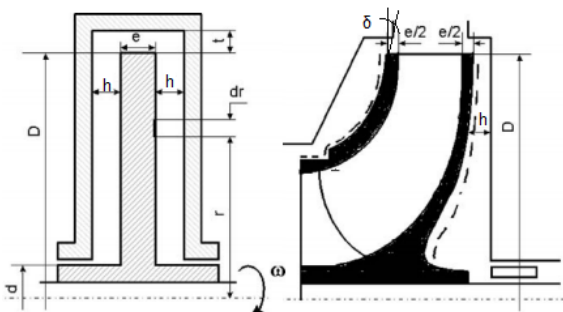


**Fig. 1.** Geometry of the simplified case and real impeller [8].

Although the governing parameters for disk friction losses were identified, the derived equations are valid only for simple disk geometry and their usability in turboma-

\*e-mail: lucie.zemanova1@vut.cz

chinery applications is limited. GÜLICH [1] described variables on impeller, which plays decisive role in disk friction losses in real pumps, as is shown in Fig. 1 right. Effect of Reynolds number, surface roughness and axial gap in connection with realistic shapes used in turbomachinery were studied, e. g. in [7–9]. Beside the mentioned parameters, disk friction is influenced by the shape of the stator and sidewall gaps, leakage flow, partload recirculation and exchange of momentum, which can be altogether hardly expressed by a single formula [1].

However, in these days, we are able to use methods, which can overcome the problem and all mentioned phenomena can be computationally captured using CFD. Not only friction losses (efficiency) calculations, but detailed insight into flow patterns in the whole pump domain can be obtained by CFD. Considering the main pump fluid regions, the methodology of such analyses is described in many studies, e.g. [9–13].

In the vast majority of the simulations of flow inside the pumps, models based on Reynolds-Averaged Navier-Stokes equation (RANS) are used due to its optimal ratio of sufficient accuracy and computational resources. SST k- $\omega$  and k- $\varepsilon$  Realizable are the most common and in many cases justified turbulence models. The most of the CFD studies neglects the influence of sidewall gaps on the global flow and the regions of front and back side disk gaps are not involved into the simulation at all, as can be seen in [9–13]. The studies, where it is included [14, 15], do not show any special approach in order to resolve the flow in those regions. Moreover, the mesh in the narrow gaps has often low quality and no attention is paid to these domains, although it was shown, that it can significantly change the performance of the pump [15].

The flow in the sidewall gaps can be very complex. Dependent on the dimensions of the gap (height  $h$ , diameter  $D$ ), and operating conditions (angular velocity  $\omega$ , flow rate  $Q$ ), four mentioned flow regimes can occur. Dimensionless numbers used for description of the regimes are aspect ratio  $G$ :

$$G = \frac{h}{D} \quad (2)$$

and rotational Reynolds number  $Re$ :

$$Re = \frac{\omega D^2}{\nu} \quad (3)$$

Additionally, several types of vortex structures can emerge in boundary layers during transitions from one regime to another. Complex overview of it including conditions where it appears published Launder et al. [16]. It can take a form of spirals rotating in the same or opposite direction than the disk, concentric circular rolls or turbulent spots, as describes [17, 18] and shows Fig. 2.

It has to be pointed out, that modelling of the flow between stationary and rotating disks is quite challenging task for CFD. Due to the complexity of the flow patterns, achieving a realistic description is not a trivial task. There were many approaches to calculate velocity components inside the rotating cavity. Chew [19] used k- $\varepsilon$  turbulence model with wall functions, Poncet et al. [20]

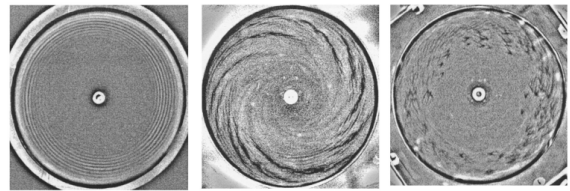


**Fig. 2.** Different types of unstable structures [17].

solved the flow by SST k- $\omega$ . Promising results described Elena and Schiestel [21] using RSM. Soghe et al. discussed the differences between results obtained by low- and high- Reynolds approach of modelling near wall regions. More detailed studies were based on direct numerical simulation (DNS), e. g. [22, 23], or large eddy simulation (LES) [24, 25].

Capabilities of particular turbulence models to describe the flow between stationary and rotating disk were published in a previous study [26]. It was found out, that simpler and less computationally demanding RANS models can provide a reasonable solution for base flow, however, they are not able to capture instabilities in boundary layers. Even low-Reynolds approach and hybrid models (Detached Eddy Simulation, Scale Adaptive Simulation) were not able to resolve the boundary layers correctly. Comparison of radial and tangential velocities revealed, that all models are compliant in the core of the fluid. Nevertheless, significant discrepancies can be observed in the near wall regions. These areas are important for the onset and spreading of instabilities. Above that, velocity profiles in boundary layers are crucial for precise determination of the dissipation on the shroud and the hub (disk friction losses).

Following study demonstrates CFD analysis of centrifugal pump with emphasis on the flow inside impeller sidewall gaps. Based on previous knowledge, LES approach is necessary to resolve the boundary layers in those regions correctly. Using LES in the whole domain of the pump would require extreme computational resources. In order to obtain accurate results in reasonable time, embedded LES approach combining Large Eddy simulation in the sidewall gaps and RANS model in the rest of the fluid was used.

## 2 Numerical simulation - simplified rotating cavity

Before the calculation of the whole pump, flow inside simplified disk cavity with throughflow was solved to verify embedded LES approach and its capability to detect instabilities on simpler geometry. The findings were then applied on the complex geometry of the radial pump. All simulations were done using ANSYS 19.1 software, meshes were created by ANSYS Meshing.

### 2.1 Geometry and mesh

The geometry of the test case was based on the same geometry of rotating cavity as in experimental study [27] and

preliminary numerical investigation [26], where instabilities were observed. The main dimensions were kept, inlet and outlet non-rotating domains were added, as shown Fig. 3. Due to the symmetry of boundary conditions and the resulting flow, it was possible to reduce the domain to the fraction to save computational resources [27], therefore, 1/8 of the geometry was taken into account.

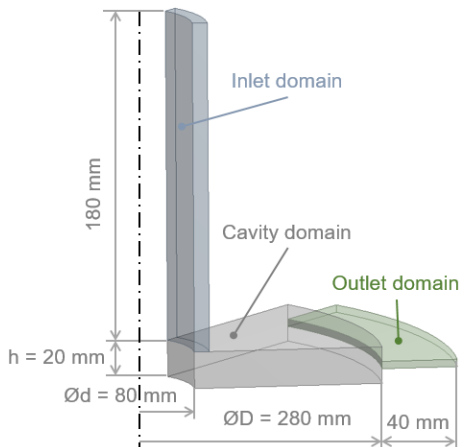


**Fig. 3.** Geometry and dimensions.

The mesh meeting requirements for LES was generated in the cavity domain. The spatial resolution was  $(200 \times 80 \times 120)$  elements in radial, tangential and axial direction with refinements near walls to comply  $y^+ \approx 1$ . For inlet and outlet domain, high-Reynolds turbulence model was applied, thus the requirements on element sizing were not so strict. Refinements in near wall regions were applied to achieve  $y^+ \approx 30$ . The whole mesh was conformal, made up of 1 960 000 hexa elements.

## 2.2 Boundary conditions

Boundary conditions are schematically shown in Fig. 4. There were 3 cell zones, as mentioned before.

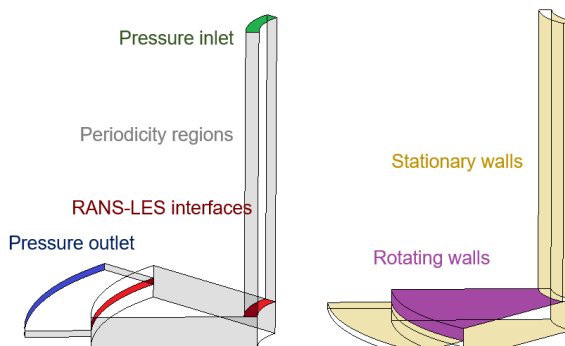


**Fig. 4.** Boundary conditions.

Inlet and outlet domain were RANS zones, while cavity domain was LES zone. Therefore, RANS-LES interfaces needed to be set up to connect them. These interfaces

are conformal and are marked in red in Fig. 4. Grey regions represent periodic boundary condition. Pressure inlet and pressure outlet with gauge pressure = 0 Pa were applied on the borders of the domain. No-slip boundary condition was applied to all of the walls of the cavity. Upper part (violet) was rotating, whilst the rest of the walls was stationary. To achieve unstable structures in the boundary layer, for the cavity with given dimensions (aspect ratio  $G = 5$ ), Reynolds number has to be  $Re = 4 \times 10^5$ . It corresponds to angular velocity  $\omega = 20.4082 \text{ rad.s}^{-1}$ .

## 2.3 Computational details and solver settings

The default model for liquid water from ANSYS library was used. It was considered incompressible. The calculation was in the first step run as steady-state with  $k-\epsilon$  Realizable turbulence model in the whole domain. For pressure-velocity coupling, SIMPLE scheme was used with the first orders of accuracy for advection terms in all transport equation. Non-equilibrium wall functions were used to resolve boundary layer regions. After achieving the convergence, simulation was switched to transient. Embedded LES approach was applied by changing the cavity domain to LES zone, while the rest of the domain was kept RANS. Embedded subgrid-scale model WALE was used with bounded central differencing momentum spatial discretization scheme. The accuracy was switched to second orders for all transport equations and pressure-velocity coupling algorithm was changed to PISO according to recommendation for unsteady cases. This procedure was tested and proved in previous study [26]. With respect to physical nature of the unstable structures and previously reported numerical results [26, 27], time step was set to  $\Delta t = 1 \times 10^{-5} \text{ s}$ .

## 2.4 Results

The ability to capture coherent vortices in boundary layers of rotating cavity by embedded LES approach was confirmed. Q-criterion was used for visualisation. This metric is commonly used, e. g. in [24, 25], to track unstable flow structures and it was also successfully incorporated in previous study [26]. As shows Fig. 5, so-called Type II instability emerging in form of spirals can be clearly observed and therefore it was proved, the approach can be used for precise modelling of the flow in sidewall gaps of centrifugal pump.

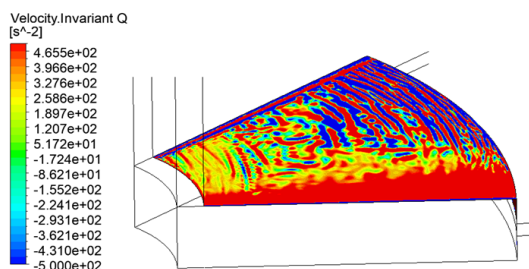


**Fig. 5.** Instabilities of boundary layer captured by Q-criterion.

### 3 Numerical simulation - radial centrifugal pump

The flow in centrifugal radial pump was defined by parameters in Tab. 1. It belongs to the best efficiency point (BEP).

**Table 1.** Parameters of the pump at BEP.

<b>Number of blades <math>z</math> (-)</b>	6
<b>Average value of blade angle <math>\beta_2</math> (<math>^{\circ}</math>)</b>	60
<b>Impeller diameter <math>D_2</math> (m)</b>	0,174
<b>Flow rate <math>Q</math> (<math>l \cdot s^{-1}</math>)</b>	31
<b>Specific energy <math>Y</math> (<math>J \cdot kg^{-1}</math>)</b>	329
<b>Rotational speed <math>n</math> (<math>s^{-1}</math>)</b>	48,3
<b>Specific speed <math>n_s</math> (<math>s^{-1}</math>)</b>	128

#### 3.1 Geometry and mesh

The inner geometry of the pump was divided into 5 domains, which are shown in Fig. 6. They were meshed separately and then merged within preprocessing in Fluent.



**Fig. 6.** Instabilities of boundary layer captured by Q-criterion.

Inlet domain was meshed using ANSYS Meshing with fully hexa mesh, wall refinements were set in order to use RANS turbulent model there. Impeller geometry was

made using BladeGen and meshed by TurboGrid meshing tool. Volute consisted of tetra mesh with prismatic boundary layer and was created in ANSYS Meshing. Sidewall gaps were meshed in ANSYS Meshing as well with hexa elements and special impact on quality of the mesh, since  $y^+ \approx 1$  was necessary to obtain in order to use LES in those regions. The whole mesh was merged by 5 non-conformal interfaces and consists of approximately 14 500 000 cells. Some details can be seen in Fig. 7.

#### 3.2 Boundary conditions

No-slip boundary condition was applied to the walls. The fluid enters the domain in mass flow inlet which is shown in Fig. 8, where for BEP mass flow rate corresponds to  $31 \text{ kg} \cdot \text{s}^{-1}$ . The domain of impeller rotates, while the others are stationary and only walls adjacent to the impeller are treated with rotational wall boundary condition. The rotational speed of the impeller and surrounding walls was set to  $n = 2900 \text{ rpm}$ . There are two pressure outlets according to Fig. 8. The first belongs to the volute, where  $p = 434\,793 \text{ Pa}$  obtained from measurement was prescribed. The second pressure outlet with atmospheric pressure is in the shaft region of the backside gap domain. The individual domains are coupled together by interfaces. Sliding mesh type of interface was used in inlet - impeller and impeller - volute regions, while at volute - frontside gap, volute - backside gap and frontside gap - inlet, RANS-LES interfaces were established.

#### 3.3 Computational details and solver settings

Material properties of liquid water were used from ANSYS Fluent library as well as in previous case, it was treated as incompressible fluid. In RANS domains, k- $\epsilon$  Realizable turbulence model was set, front- and back-side gaps of special interest were computed by LES. WALE subgrid-scale model recommended for embedded LES approach was used. Common practice in CFD in turbomachinery is to set such a time step, which ensures rotation of max  $2^{\circ}$  per  $\Delta t$ . The time step was finally even lower ( $\Delta t = 1 \times 10^{-6} \text{ s}$ ) in order to fulfill the Courant-Friedrichs-Lowy (CFL) condition. The transient analysis was initialized from converged steady results. First orders of accuracy were first set and after achieving convergence for transient case it was switched to the second orders.

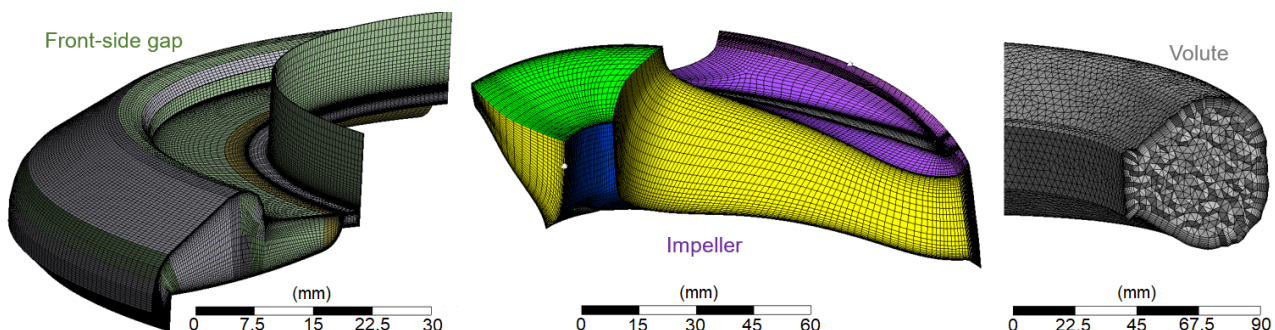


**Fig. 7.** Details of mesh.

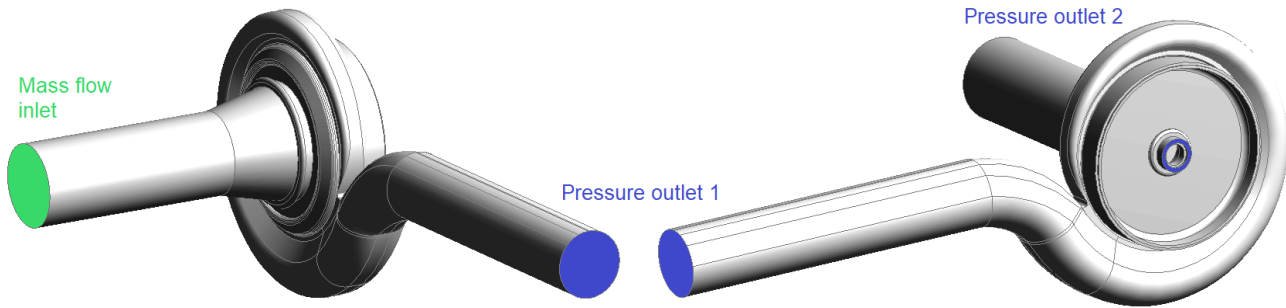


**Fig. 8.** Boundary conditions.

### 3.4 Results

The flow inside the pump is very complex and moreover, changes in time with rotation of the impeller. Pressure and velocity in particular point of front-side or back-side gap domain depend on current position of blades. Typical example of overall velocity field in one meridional section shows Fig. 9.

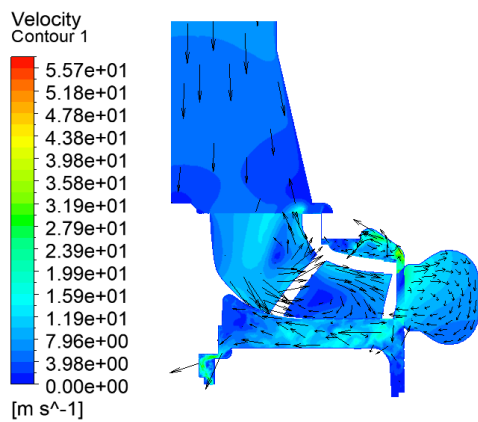


**Fig. 9.** Vectors of velocity in meridional section.

As a consequence of shape of pump spiral casing, blades passing the volute cutwater produce pressure pulsations. They are well observable on pressure contours on the front-side gap wall. Another effect is that in some circumferential locations, the water flows into the sidewall gaps, whereas in other positions flow of opposite direction occurs. It also causes very diverse velocity field at the entrance to the sidewall gap. Fig. 10 demonstrates it on the velocity vectors and pressure distribution at the interface between the impeller domain and front-side gap domain.

As the impeller rotates, the direction of the flow into and out of the sidewall gaps changes periodically with passing blades. Fig. 11 shows the changes during 8 time steps corresponding to 1/6 of impeller revolution (1 blade passes the volute cutwater).

The uneven velocity around the entrance into the front-sidewall gap results in very complex flow field in this region. Strong vortical structures of various shapes emerge in the whole domain, as shows Fig. 12.

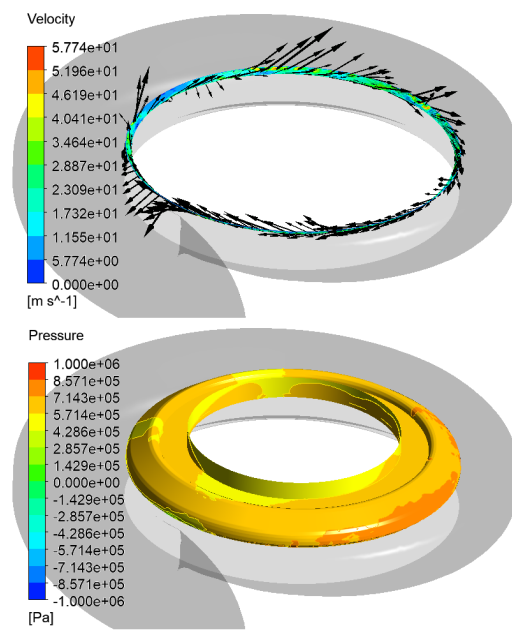


**Fig. 10.** Vectors of velocity at the interface and pressure distribution in front-side gap.

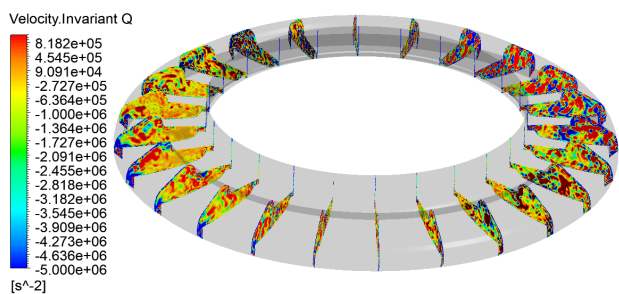


**Fig. 12.** Q-criterion in front-side gap.

Furthermore, the flow field evolves in time with rotation of the impeller. Fig. 13 shows evolution of radial and tangential components of velocity measured in the middle of the cross section of the front-side gap. Typical S-shaped radial and tangential velocity profiles known from simplified disk in cylindrical cases are highly distorted due to the complicated shape of the spiral casing.

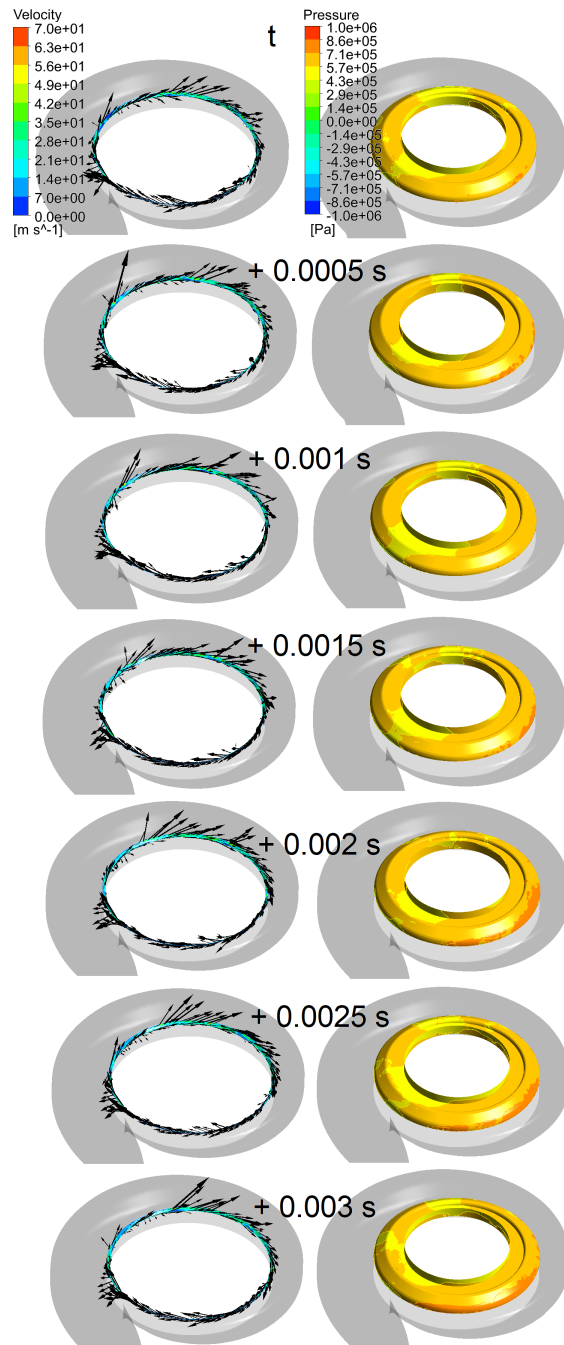


**Fig. 11.** Velocity and pressure evolution during 1 blade passage.

Analogical situation appears in back-side gap. Again, the flow field is uneven and is strongly influenced by position of blades and volute cutwater. Depending on the circumferential position, the water either flows in or out of the gap, as can be seen in Fig. 14 top. The rotation of the impeller is also accompanied by non-constant pressure distribution and pressure pulsations in time, as shows Fig. 14 bottom.

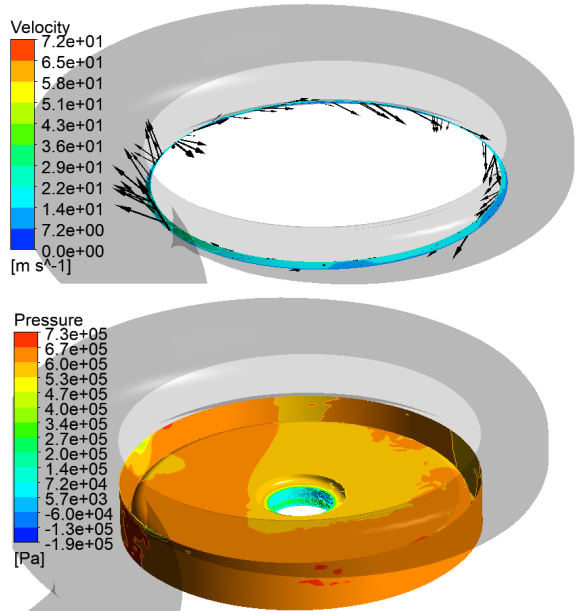


**Fig. 14.** Vectors of velocity at the interface and pressure distribution in back-side gap.

Such operating conditions result in strong whirls in back-side gap, as documents Q-criterion visualisation in Fig. 15. Taking into consideration only outer diameter, gap width and angular velocity of the impeller, according to stability diagram by Daily and Necce [2], flow regime IV with turbulent separated boundary layers should occur in both sidewall gaps, transitions or vortices should not be visible. However, the results suggests, that this approach would be unjustified simplification for the case of real impeller rotating in spiral casing. The changes of velocity in circumferential direction due to shape of casing and in time as a consequence of impeller rotation lead to more complicated evolution of the flow field in sidewall gaps.

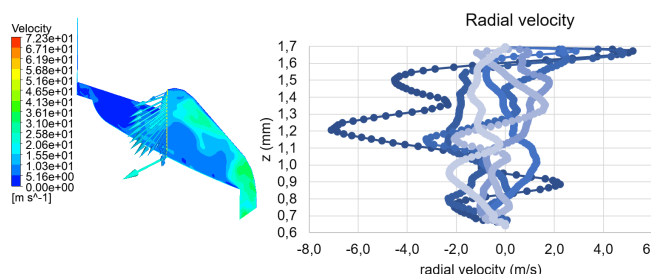


**Fig. 13.** Radial and tangential velocity in time during 1 blade passage.

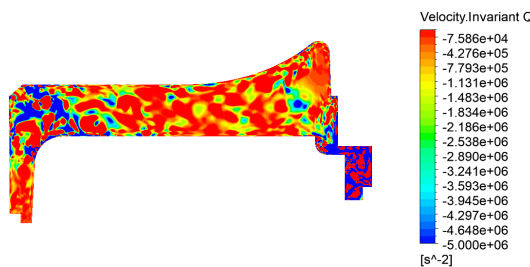


**Fig. 15.** Q-criterion in back-side gap.

During experiment, pressure in 3 radial positions was measured using pressure probes. Their locations are shown in Fig. 16, where can be seen comparison with CFD results as well. Measured and calculated values summarizes Tab. 2. Quite large discrepancy is apparent. It is probably caused by different procedure of evaluation experimental and calculated data. Experimental data were collected for a period of time (several impeller turns) and average value was taken into account, while due to lack of numerical data for such a time interval, average value from circle of given radius was considered. The trend is similar, however absolute values differ significantly.

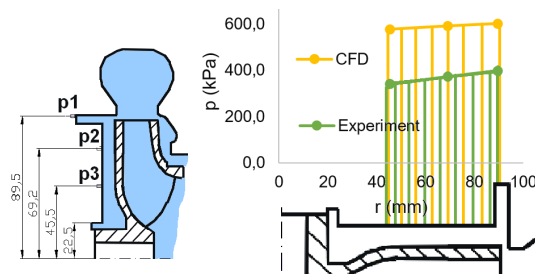


**Fig. 16.** Pressure acting on the back sidewall gap.

**Table 2.** Comparison of calculation with experiment.

	Experimental (time averaged)	Simulation (domain averaged)
<b>p1 (kPa)</b>	397.9	602
<b>p2 (kPa)</b>	372.8	591.7
<b>p3 (kPa)</b>	340.3	578

The insight into complex flow inside front and back-side wall cavities can be used with benefits for precise determination of disk friction. Comparison of friction moments on hub and shroud calculated using empirical equations and CFD simulation shows Tab. 3. The CFD simulation was performed without consideration of surface roughness, thus smooth surface was taken into account also in empirical calculations in order to compare the results.

**Table 3.** Comparison of friction moments.

	Empirical	Simulation
<b>M shroud (<math>N \cdot m</math>)</b>	0.493	0.5
<b>M hub (<math>N \cdot m</math>)</b>	0.422	0.235
<b>M total (<math>N \cdot m</math>)</b>	0.915	0.735

Very good agreement is achieved in terms of disk friction on shroud. It probably results from relative geometry simplicity of back-side gap, which is close to the model example of disk against flat casing. The gap width is constant in the major part of the domain. The cross-section of front-side gap is more complicated, the gap width is not constant and the shape is not very similar to the geometry for which the empirical relationships were derived. Therefore, the resulting discrepancy is larger. It is then pronounced into the total friction moment.

#### 4 Conclusions

Using of CFD for precise determination of flow field in sidewall gaps was demonstrated on practical application of radial pump. It was proved, that Embedded LES approach is capable of capturing swirling flow in narrow gaps between rotor and stator not only for simplified cases, but also when considering the real pump geometry.

The results suggest, that the flow in sidewall gaps is quite complex and unstable. Fully transient analysis is required in order to describe the flow field sufficiently. The velocity and pressure changes in time with rotation of the impeller and also in space, which excludes the use of periodic boundary condition for subsequent analysis. To obtain proper results, non-axisymmetry of the volute is necessary to take into account.

It was shown, that as the impeller rotates, the direction of flow into and out of the both sidewall gaps periodically changes with passages of blades through area of volute cutwater. It also causes pressure pulsations, which are also well observable in both sidewall gaps domains.

For better comparison with experimental data, more calculated time steps (corresponding to few turns of the impeller) would be necessary.

Experimental data in order to compare friction moments on disks are not available, thus approximate empirical equations which are commonly used in turbomachinery were considered. They are in good agreement with CFD in case of shroud resulting from relative simplicity of the back-side gap geometry which is close to the theoretical cylindrical cavity. In estimation of the disk friction loss on the hub, simplified equations are not very precise. The cross-section is more complicated and the error propagates further to the total friction moment. In such complex geometries, CFD simulation is more appropriate tool for precise estimation of disk friction losses.

Research was supported by project of Ministry of Education, Youth and Sports of the Czech Republic LTARF18019 and by project of BUT FME FSI-S-17-4615.

## References

1. J. F. GÜLLICH, Forschung im Ingenieurwesen, **68**, 87–95 (2003)
2. J. W. Daily and R. E Nece, J. of Basic Eng. **82**, 217–230 (1960)
3. R. E. Nece and J. W. Daily, J. of Basic Eng. **82**, 553–560 (1960)
4. D. Coren et al., Proc. of the Institution of Mech. Eng., **223**, 873–888, (2009)
5. B. Hu et al., Int. J. of Turbomachinery, Propulsion and Power, **2**, (2017)
6. B. Hu et al., Int. J. of Turbomachinery, Propulsion and Power, **3**, (2018)
7. S. Mikhail et al., ICFDP7, (2001)
8. A. Nemdili and D. H. Hellmann, The 6th Int. Conf. on Hydraulic Machinery and Hydrodynamics, 235–240, (2004)
9. L. Cho et al., Transactions of the Japan Society for Aeronautical and Space Sci., **55**, 150–156, (2012)
10. K. Matsumara et al., IOP Conf. Ser. Earth Environ. Sci., **240**, (2019)
11. E. Dick et al., Task quarterly, **5**, 579–594, (2001)
12. S. Deniz et al., IOP Conf. Ser. Earth Environ. Sci., **240**, (2019)
13. S. R. Shah et al., Proc. Eng., **51**, 715–720, (2013)
14. S. Yang, et al., Renewable Energy, **48**, 507–513, (2012)
15. A. Ayad et al., Aerospace Sc. and Tech., **47**, 247–255, (2015)
16. B. Launder et al., Annual Rev. of Fluid Mech., **42**, 229–248, (2010)
17. A. Cross and P. Le-Gal, Physics of Fluids, **14**, 3755–3765, (2002)
18. L. Schouveiler et al., Experiments in Fluids, **26**, 179–187, (1999)
19. J. W. Chew, Int. J. of Turbo and Jet Engines, **2**, 253–262, (1985)
20. S. Poncet et al., ECCOMAS CFD 2010, (2010).
21. L. Elena and R. Schiestel, Int. J. of Heat and Fluid Flow, **17**, 283–289, (1996)
22. E. Serre et al., J. of Fluid Mech., **434**, 65–100, (2001)
23. E. Tuliska-Sznitko at al., Comptes Rendus Mécanique, **330**, 91–99, (2002)
24. R. Pasquetti et al., Theoretical and Computational Fluid Dynamics, **22**, 261–273, (2008)
25. E. Séverac and E. Serre, J. of Computational Physics, **226**, 1234–1255, (2007)
26. L. Zemanová and P. Rudolf, Proc. of the Int. conf. Experimental Fluid Mechanics 2018, 705–712, (2018)
27. S. Viazzo et al., Flow, Turbulence and Combustion, **88**, 63–75, (2012)